Biominerals Formed by DNA and Calcium Oxalate or Hydroxyapatite: A Comparative Study

Guillem Revilla-López,[1] Anna M. Rodríguez-Rivero,[2,3] Luis J. del Valle,[1,4] Jordi Puiggalí,[1,4,5] Pau Turon[2,*] and Carlos Alemán[1,4,5,*]

[1] Departament d'Enginyeria Química, EEBE, Universitat Politècnica de Catalunya, C/Eduard Maristany 10-14, Edif. I2, 08019 Barcelona, Spain

[2] Research and Development, B. Braun Surgical, S.A. Ctra. de Terrassa 121, 08191 Rubí, Barcelona, Spain

[3] Universitat Autònoma de Barcelona. Campus de la UAB, Plaça Cívica, 08193 Bellaterra, Barcelona, Spain

[4] Barcelona Research Center for Multiscale Science and Engineering, EEBE, Universitat Politècnica de Catalunya, C/Eduard Maristany 10-14, Edif. C, 08019 Barcelona, Spain

[5] Institute for Bioengineering of Catalonia (IBEC), The Barcelona Institute of Science and Technology, Baldiri Reixac 10-12, 08028 Barcelona, Spain

[*] Correspondence to: pau.turon@bbraun.com and carlos.aleman@upc.edu

ABSTRACT

Biominerals formed by DNA and calcium oxalate (CaOx) or hydroxyapatite (HAp; the most important and stable phase of calcium phosphate) have been examined and compared using a synergistic combination of computer simulation and experimental studies. The interest of this comparison stems from the medical observation that HAp- and CaOx-based microcalcifications are frequently observed in breast cancer tissue and some of their features are used as part of the diagnosis. Molecular dynamics simulations show that: 1) the DNA double helix remains stable when it is adsorbed onto the most stable facet of HAp, whereas it undergoes significant structural distortions when it is adsorbed onto CaOx; 2) DNA acts as template for the nucleation and growth of HAp but not for the mineralization of CaOx; 3) the DNA double helix remains stable when it is encapsulated inside HAp nanopores but it becomes destabilized when the encapsulation occurs into CaOx nanopores. Furthermore, CaOx and HAp minerals containing DNA molecules inside and/or adsorbed on the surface have been prepared in the lab by mixing solutions containing the corresponding ions with fish sperm DNA. Characterization of the formed minerals, which has been focused on the identification of DNA using UV-vis spectroscopy, indicates that the tendency to adsorb and, especially, encapsulate DNA is much smaller for CaOx than for HAp, which is in perfect agreement with results from MD simulations. Finally, quantum mechanical calculations have been performed to rationalize these results in terms of molecular interactions, results evidencing the high affinity of Ca^{2+} towards oxalate anions in aqueous environment.

INTRODUCTION

The combination of DNA with nanomaterials (*e.g.* gold and metal oxide nanoparticles, carbon-based nanomaterials and minerals) to form hybrid systems is of fundamental interest for applications in DNA delivery, biosensors development and nanotechnology.[1-8] Within this extensive field of research, the interaction of DNA with nanostructured calcium phosphate (CaP) is especially relevant because of its important biological implications. In particular, hydroxyapatite (HAp), which is probably the most important phase of CaP, is the main mineral of mammalian tooth enamel and bone,[9] where it grows as nano-sized mineral platelets at nucleating sites on a protein template.[10,11] Understanding the interaction between HAp and DNA has been found to be essential for biomedical field applications. For example, HAp nanoparticles (NPs) have been used for cell transfection as carrier of nucleic acids[12-15] and for purifying DNA from virus.[16]

On the other hand, spectroscopic studies on HAp microcalcifications formed inside living organism (*i.e.* tumoral tissue) showed the contribution of vibrational modes of DNA, phospholipids and proteins.[17] Such finding is particularly relevant since HAp detection in breast cancer microcalcifications have been successfully used for screening and diagnosis purposes.[18-20] More specifically, such analyses concentrated on the chemical differentiation between two minerals: calcium oxalate (CaOx), usually associated with benign prognosis, and HAp, which is more frequently associated with malignancy.[21,22]

In recent years the interaction between plasmid DNA and both nanostructured HAp, $Ca_{10}(PO_4)_6(OH)_2$, and amorphous CaP has been examined.[23-28] Results showed that DNA adsorption depends on the HAp morphology, NPs and fusiform nanorods adsorbing more DNA than flower-like and laminar nanocrystals.[23] Similar results were

obtained for polyphosphates, which mimicked the backbone of DNA.[24] Structural changes induced in plasma DNA by the adsorption on HAp resulted in an enhanced stabilization, increasing the resistance against enzymatic digestion.[23] Besides, the formation of HAp was found to be regulated by DNA, which acts as a template in a "*biomineralization*" process.[25-28] More specifically, the DNA backbone behaved as a very large nucleus for the growth of HAp surrounding the biomolecule.[28] Moreover, the utilization of HAp NPs as non-viral vectors for transfection has been demonstrated, proving that such inorganic particles are able to deliver DNA or RNA to a cell.[23,29-31] Interestingly, Mg^{2+} was found to play a unique role in the DNA-HAp biomineralization process since this ion has a very high affinity towards DNA, whereas in the initial stages of the particle nucleation process it prefers to be located at the surface regions rather than at the core ones.[32]

This work renders a physical-chemical explanation to a long term debate in the medical community regarding if and why breast cancer patients with HAp-based micro-calcifications have a worse prognosis compared to those showing mostly CaOx-based micro-calcifications. The first part of the paper deals with the energetics and statistical mechanics of mineral···DNA complexation and the second part proves that DNA can only be encapsulated without denaturalization in HAp-based matrices thus forming biominerals not only able to encapsulate and transport DNA but also to deliver it.[33] For this purpose, we have used a synergistic approach to compare DNA mineralization in HAp and CaOx. Particularly, the capacity of DNA to interact with HAp and CaOx has been examined theoretically and experimentally. Initially, molecular dynamics (MD) simulations have been carried out in order to analyze: the adsorption of DNA onto the most stable facet of HAp and CaOx, the growing of HAp and CaOx minerals around the DNA template (*i.e.* the nucleating effect of DNA), and the stability of biominerals

formed by DNA encapsulated inside nanopores of HAp or CaOx. After this, DNA-CaOx and DNA-HAp complexes have been synthesized in the laboratory and studied by UV-vis spectroscopy to compare the ability of these minerals to adsorb and encapsulate DNA. Finally, quantum mechanical (QM) calculations have been conducted to provide a comprehensive chemical explanation of the results derived from both MD simulations and UV-vis spectroscopy, which are fully consistent. It is worth mentioning that special attention has been given to the discussion of the biominerals involving CaOx, which have been much less studied than those that contain HAp, and to the role of Mg^{2+}.

METHODS

Molecular dynamics

MD simulations were performed with the NAMD 2.6 software package.[34] In order to study the adsorption and encapsulation of DNA in CaOx and HAp, we took into consideration the clinical interest of hypomethylated and hypermethylated DNA sequences as they have been associated with the overexpression of genes or genes silenced linked to cancer disease.[35-38] More specifically, two representative DNA dodecamers were selected to cover the full range of methylation: a) the highly methylated dodecamer 5'-CG^{4}GTCG^{5}CCG^{6}TCG^7-3' (hereafter R1A) extracted from the RASSF1A gene; and b) the Dickerson dodecamer 5'-CGCGAATTCGCG-3' (hereafter DD) as representative of unmethylated sequences. The DD is widely used as DNA probe in experiments, working as a wildcard when no specific sequence is investigated. On the other hand, hypermethylation of the RASSF1A gene has been correlated with clinical and pathological characteristics of breast cancer and with clinical outcomes.[39] Charge neutralization was performed with the addition of Mg^{2+} counterions, which were located at the major groove of the double helix.[40]

Force-field parameters for DNA and phosphate anions were taken from ff99-SB,[41] Ca^{2+} parameters were from Bradbook *et al.*[42] and parameters for Mg^{2+} were from Sorensen *et al.*[43] The TIP3P[44] water model was employed to describe explicit water molecules. In previous work we used quantum mechanical calculations on model systems to demonstrate that such combination of force-field parameters satisfactorily reproduce the interactions of DNA···HAp systems.[25] Bonding and van der Waals parameters for oxalate anions (Ox^{2-}) were extracted from the general Amber force-field gaff,[45] while charges were developed following the RESP[46] protocol and using *ab initio* HF/6-31G* calculations.

All productive MD runs were performed in the NPT ensemble at 298 K and 1 bar. Both temperature and pressure were controlled by the Berendsen thermobarostat.[47] Productive MD simulations were conducted using an integration time step of 2 fs. Representative structures were extracted every 500 steps. Van der Waals interactions were evaluated with a cut-off of 10 Å and a switching distance at 8 Å. For electrostatic interactions, we computed the non-truncated electrostatic potential throughout Ewald Summations, *i.e.* the Particle-Mesh Ewald (PME) method.[48] The real space term was determined by the van der Waals cut-off (10 Å), while the reciprocal term was estimated by interpolation of the effective charge into a charge mesh with a grid thickness of 5 points per volume unit. In all cases bond lengths involving hydrogen were kept frozen by using the SHAKE algorithm.[49]

Adsorption of DNA. The HAp hexagonal unit cell with $P6_3/m$ geometry (a= b= 9.421 Å, c= 6.881 Å, α= β= 90º, and γ= 120º) and the 4e Wyckoff position occupied by two hydroxyl ions, each with ½ occupancy,[50] and the monohydrated CaOx monoclinic unit cell with $P2_1/c$ geometry (a= 6.316 Å, b= 14.541 Å, c= 10.116 Å, α= γ= 90º, and β= 109º)[51] were generated. These systems were cleaved to obtain the most stable facet of

such minerals (see below). HAp and CaOx unit cells were expanded 6 and 4 times in the *x* and *y* directions, respectively, creating 6×6 and 4×4 supercells. The thickness of the supercell in the *z* axis entailed a 4 and 2 layer slab for HAp and CaOx, respectively. Afterwards, both surfaces were solvated in the *z* direction with 17756 and 12532 water molecules for the (001) of HAp and the (100) of CaOx, respectively.

Initially, water and DNA coordinates were optimized through 5000 steps of conjugated gradient algorithm minimization. The resulting coordinates of the two systems underwent 0.5 ns of NVT molecular dynamics (MD) at 373 K with frozen coordinates for the DNA and the mineral. Final coordinates and velocities of the NVT run were used as input for 0.5 ns NPT (298 K, 1 bar) to equilibrate energy and water density (to 1 g/cm^3) in the volume occupied by the liquid and the DNA. The Berendsen thermobarostat[47] was employed at constant *xy* plane area and frozen DNA and mineral slab coordinates. Productive dynamics started from the latter output, only keeping fixed the mineral atoms. Trajectories were 150 ns long.

DNA in solution. The R1A and DD double helices and Mg^{2+} counterions were solvated with 30000 water molecules and the density of the resulting system was equilibrated to 1 g/cm^3 following the same protocol used for the surface slabs in the adsorption simulations. Productive control dynamics were 150 ns long.

Nucleation of DNA biominerals. As DNA methylation is not expected to play any role in the nucleation of biominerals, simulations were conducted using the R1A dodecamer only. The nucleation of CaOx around R1A was simulated considering, in addition of the dodecamer, 10 Mg^{2+}, 20 Ca^{2+}, 20 Ox^{2-} molecules and 50551 water molecules. The nucleation of HAp around the R1A was examined considering a system with 10 Mg^{2+}, 30 Ca^{2+}, 20 PO_4^{3-} molecules and 51675 water molecules.

Systems were previously equilibrated at the target temperature (298 K), pressure (1 atm) and density (1 g/cm^{-1}). For this purpose, 5000 steps of energy minimization were initially performed to relax structural tensions. After this, solvent and ions were thermally relaxed by three consecutive runs, while the B-DNA was kept frozen: 0.5 ns of NVT-MD (volume conserved) at 500 K were used to homogeneously distribute the solvent and ions in the box. Then, 0.5 ns of isothermal (298 K) and 0.5 ns of isobaric (1 atm and 298 K) relaxations were run. Finally, all the atoms of the systems were submitted to 0.15 ns of steady heating until the target temperature was reached (298 K), 0.25 ns of NVT-MD at 298 K (thermal equilibration), followed by 0.5 ns of density relaxation (NPT-MD). After equilibration, productive MD simulations of 150 ns were conducted.

Encapsulation of DNA. The HAp hexagonal unit cell[50] and the monohydrated CaOx monoclinic unit cell[51] were used to construct super-cells considering 6×6×7 and 4×4×5 unit cells, respectively. After this, a hole was generated in the centre of each super-cell, the dimensions of such hole being defined by DNA double helix. After several trials, we found that a hole of 2×2×7 units cells was the minimum required for both minerals to accommodate the double helix without severe steric contacts. In order to completely avoid unfavorable steric interactions between the apatite and the biomolecule, some additional atoms and groups of atoms were translated at their border regions allowing us to maintain the electroneutrality of the super-cells. Then, R1A and DD double helices, which were arranged in the canonical B form, were embedded inside the pores. In order to maintain the electrical neutrality of the system, Mg^{2+} ions were put at the major groove of the double helix. Figure 1 depicts the starting models used to represent DD double helix embedded into HAp and CaOx pores, starting models for the R1A sequence being analogous to these ones.

In order to evaluate the stability of the encapsulated DNA models, both energy minimization and MD simulations were applied. Initially, all the models were minimized by applying 5×10^3 steps of steepest descent to relax the more important conformational and structural tensions. Then, a MD run of 3.0 ns in the NVT ensemble (constant number of particles, volume and temperature) at 298 K was carried out to equilibrate the four systems under study (*i.e.* R1A and DD encapsulated into HAp and CaOx) and eliminate small structural tensions. After such thermal relaxation, the saved coordinates were submitted to a new energy minimization by applying 5×10^3 steps of steepest descent until energy convergence. In both energy minimizations and MD simulation, atoms contained in R1A and DD were only allowed to move from their positions, the coordinates of the mineral being kept fixed at their crystallographic positions in all cases. Each system was calculated in triplicate considering starting points that differ in the orientation of the DNA inside the generated holes.

In vitro synthesis of biominerals

In vitro synthesis of DNA-CaOx and DNA-MgOx complexes. The synchronized dropwise (rate of 2 mL/min) addition of 10 mL of a solution of 0.04 M sodium oxalate (Sigma Aldrich 99,5%, 223433) and 10 mL of 0.04 M $CaCl_2$ (Scharlab, CA01920500) to 0.06 g of fish sperm DNA (Sigma Aldrich, 74782) was conducted under stirring at 75 ºC for 5 h. Then, the resulting solutions were cooled to room temperature, centrifuged and washed successively with molecular biology grade water (Millipore, H2OMB0506) twice and a 60/40 v/v mixture of ethanol–water (Ethanol, Scharlab ET0011000). A white powder with traces of pale orange was obtained after freeze-drying. Calcium chloride was replaced by $MgCl_2$ (Sigma Aldrich, M8266), to obtain the DNA-MgOx system.

In vitro synthesis of DNA-HAp complexes. 0.1 g of fish sperm DNA were added to 15 mL of a 0.3 M $(NH_4)_2HPO_4$ solution in de-ionized water. The pH of such solution was previously adjusted to 10 with aqueous ammonia. The mixture was added drop-wise (rate of 2 mL/min) and under agitation (400 rpm) to 25 mL of 0.3 M $Ca(NO_3)_2$ solution in de-ionized water and the appropriate amount of aqueous ammonia to adjust pH to 10. Temperature was maintained at 40 °C during the addition process. After that, the reaction mixture was stirred at 80 °C for 1.5h and then naturally cooled to room temperature. The resultant suspension was aged for 24 h at room temperature. Then, the precipitate was separated by centrifugation and washed sequentially with de-ionized water and a 60/40 *v*/*v* mixture of ethanol-water (twice). A white powder was obtained after freeze-drying.

A UV-3600 (Shimadzu) UV-Vis-NIR spectrophotometer controlled by the UVProbe 2.31 software was used to record UV-Vis spectra of DNA-CaOx, DNA-MgOx and DNA-HAp complexes at room temperature, in the 200-400 nm range, with a bandwidth of 0.2 nm and a scan speed of 600 nm/min.

QM calculations

QM calculations were performed using Gaussian 09 software package.[52] Geometry optimization, solvation and binding energy calculations were carried out with the hybrid functional B3LYP[53,54] combined with the 6-311G++(2d,2p) basis set. All geometry optimizations were carried out until a stationary point was reached. These were confirmed as minima by frequency analyses (*i.e.* no imaginary frequency was found). The gas-phase free energies were obtained at 298 K by correcting the energies with the zero point energy and the thermal correction term and by evaluating the entropy using standard statistical thermodynamic methods. The SMD solvation method[55] was chosen

to calculate the hydration free energy of the systems, ΔG_{hyd}, which was estimated as the difference between the free energies in the gas-phase and aqueous solution. Binding energies, ΔG_b, were calculated as $\Delta G_b = G_{sol,c} - \Sigma_i G_{sol,i}$ where $G_{sol,c}$ is the free energy of the complex in aqueous solution and $G_{sol,i}$ is the free energy of each component of the complex in aqueous solution (*i.e. i* stands for each of the interacting component of the complex). All ΔG_b values were corrected by the Base Superposition Error (BSSE) using the standard counterpoise protocol.

RESULTS AND DISCUSSION

Adsorption of DNA on the minerals surface

Initially, MD simulations were focused on the adsorption of R1A and DD sequences on the surface of the HAp and monohydrated CaOx minerals. We focused on the interaction formed when such dodecamers are adsorbed onto the most stable facet of HAp[56] and monohydrated CaOx,[57] which is the (001) and (100), respectively. Almora-Barrios *et al.*[58] reported that the calculated surface energies of the (001) and the average (010) surfaces are 1.01 and 1.32 J/m, respectively, indicating that the former is more stable than the latter, in agreement with previous literature.[59,60] Indeed, the less stable (010) surface, which was proposed to be much less populated than the (100), quickly accumulating more material that grow out of the crystal morphology because of the reactivity associated to such instability. Besides, the (100) was identified by atomic force microscopy experiments not only as the most populated facet of CaOx[61,62] but also as the surface that forms the strongest interactions with carboxylate and amidinium groups, which are abundantly present in biomolecules, including DNA.[62]

Although the methylated and non-methylated sequences showed a similar behaviour when interacting separately with HAp or monohydrated CaOx, simulations

demonstrated that the structural stability of DNA is totally different for each mineral. The stability of the adsorbed sequences was evaluated by examining the temporal evolution of the root mean square deviation (RMSD), which was calculated between each atom position of the B-DNA canonical double helix and the dodecamer structures recorded from MD trajectories. As shown below, the RMSD was converged for all systems preserving the B-DNA structure, whereas the RMSD was high enough to guarantee complete de-structuration for all systems in which the double helix is lost. However, in the latter cases convergence of the RMSD was not considered a requisite since the dynamics and structure of unfolded B-DNA is out of the scope of this work.

Figures 2a and 2b, which include the results obtained in aqueous solution (control), compare the RMSDs obtained for R1A and DD, respectively. The average RMSD obtained for R1A and DD adsorbed onto the (001) HAp (3.5±0.6 Å and 3.4±0.4 Å, respectively) is close to that obtained for the same sequence in aqueous solution (2.7±0.5 Å and 2.7±0.4 Å, respectively), evidencing that the B-DNA double helix remains stable when adsorbed onto HAp. Thus, the double helix is able to accommodate itself onto the HAp surface, independently of the methylation, by establishing a balance between the attractive and repulsive interactions between the phosphate groups of DNA and the Ca^{2+} and PO_4^{3-} ions of the mineral, respectively. The formation of such interactions is reflected in Figures 2c and S1a for R1A and DD, respectively, which display a representative snapshot of the dodecamer adsorbed onto HAp and compares the adsorbed double helix with a canonical one. The affinity of HAp towards the double helix of DNA has been attributed to the complementarity between the mineral and the phosphate groups of the DNA backbone, which were found to exhibit isomorphic planes.[25]

In contrast, the average RMSD increases progressively for the R1A and DD sequences adsorbed on the (100) facet of monohydrated CaOx, reaching in both cases values higher than 8 Å after 150 ns. Thus, the CaOx surface causes a drastic destabilization of the adsorbed double helix due to the electrostatic repulsions between the Ox^{2-} and polyphosphate DNA backbone, which are directly confronted. The effect of $Ox^{2-}\cdots$polyphosphate repulsive interactions in the double helix is illustrated in Figures 2d and S1b for R1A and DD, respectively. As it can be seen, electrostatic repulsions tend to deploy the DNA double helix, separating the two strands. This destabilizing effect is not offset by the water molecules of the internal monohydration layer, which practically does not interact with the superficial DNA.

Nucleation of DNA templated biominerals

The behavior of R1A in an ionic solution to assess the feasibility of DNA to nucleate CaOx and/or HAp biominerals and act as a template was modelled using solution-like systems containing Ox^{2-} or PO_4^{3-} ions together with the DNA dodecamer, Ca^{2+} and Mg^{2+}. Figure 3a shows the radial distribution functions (RDFs) derived from the simulation with Ox^{2-} for the following pairs: Mg^{2+}–DNA*p* (where DNA*p* refers to the centre of masses of the phosphate groups from the DNA backbone), Ca^{2+}–DNA*p*, Mg^{2+}–Ox^{2-} (where Ox^{2-} refers to the centre of masses of Ox^{2-} anions), Ca^{2+}–Ox^{2-} and DNA*p*–Ox^{2-}. For a given pair, α–β, the RDF curve gives a measure of the relative probability that β resides at a radial distance *r* from α centred at the origin of coordinates.

The profile obtained for Mg^{2+}–DNA*p* pair (black) shows a sharp peak at *r*= 1.9 Å, evidencing the high affinity of Mg^{2+} towards DNA. Besides, the first peak for the Ca^{2+}–DNA*p* pair, which appears at *r*= 2.6 Å, apparently displays a lower area

under the curve (red). On the other hand, the area under the Ca^{2+}–Ox^{2} peak at *r*= 2.6 Å (light blue) is much higher, reflecting that the attraction of Ca^{2+} by the Ox^{2-} is very favoured in comparison to the affinity by the phosphate groups from DNA. Interestingly, Ox^{2-} anions do not exhibit any affinity towards DNA, an equi-probable distribution being found once an exclusion threshold at *r*= 5.5 Å is exceeded.

Considering the possibility of forming triads like DNA*p*···X···Ox^{2-}, where X refers to Ca^{2+} or Mg^{2+} coordination ions, analysis of the RDFs shows that Ca^{2+} cannot play this role. Once Ca^{2+} is bound to DNA*p* or to Ox^{2-} prefers the interaction with surrounding explicit water molecules instead of forming the triad. Thus, the sum of the *r* values for the first peak of the Ca^{2+}–DNA*p* and Ca^{2+}–Ox^{2-} RDFs totals 5.2 Å, this value being lower than the threshold distance of cation-mediated DNA*p*–Ox^{2-} carboxyl interaction (*i.e.* 5.5 Å). The addition of the distances associated to the first peak of Mg^{2+}–DNA*p* and Mg^{2+}–Ox^{2-} RDFs renders a value of 6.0 Å, which is bigger than the cation mediated threshold. However, the absence of peaks in the RDF of the DNA*p*-Ox^{2-} pair suggests that DNA*p*···Mg^{2+}···Ox^{2-} interactions are extremely weak in highly hydrated environments. The above mentioned tendencies are reflected in Figure 3b, which displays a snapshot from the MD simulation of the modelled system (red box). As it can be seen, Ox^{2-} anions tend to form clusters with Ca^{2+} cations separated from the DNA. Apparently, the polyphosphate groups from DNA do not play any significant role in the formation of CaOx.

Figure 3c displays the RDFs derived from the simulation with PO_4^{3-} for the Mg^{2+}–DNA*p*, Ca^{2+}–DNA*p*, Mg^{2+}–PO_4^{3-} (where PO_4^{3-} refers to the centre of masses of PO_4^{3-} anions), Ca^{2+}–PO_4^{3-} and DNA*p*–PO_4^{3-} pairs. The profiles obtained for Mg^{2+}–DNA*p* and

Ca^{2+}–DNA*p* pairs (black and red, respectively) show sharp peak at *r*= 1.9 and 2.5 Å, respectively. Thus, although the affinity of the DNA dodecamer towards Mg^{2+} is higher than towards Ca^{2+}, the latter ion interacts more with the phosphate groups of DNA than in the simulation with Ox^{2-}. Besides, the Ca^{2+}–PO_4^{3-} profile shows a sharp peak at *r*= 2.5 Å (light blue), indicating that the attraction of Ca^{2+} by PO_4^{3-} anions and DNA*p* is very similar. However, the most important difference between simulations with Ox^{2-} and PO_4^{3-} is detected in the RDF calculated for the DNA*p*–PO_4^{3-} pair (green), which shows a broad peak centered at *r*= 5.00 Å. This peak evidences that PO_4^{3-} anions tend to be distributed around the DNA, which acts as a template and facilitates the growing of the mineral around it.

Moreover, in this case the formation of both DNA*p*$\cdots Ca^{2+}\cdots PO_4^{3-}$ and DNA*p*$\cdots Mg^{2+}\cdots$ PO_4^{3-} triads is consistent with the peaks observed in the RDFs. Thus, the addition of the *r* values for the first peak of the Ca^{2+}–DNA*p* and Ca^{2+}–PO_4^{3-} RDFs sums 5.0 Å, which matches the maximum of the broad peak obtained for the DNA*p*–PO_4^{3-} RDF (*i.e.* 5.0 Å). Besides, the sum of the distances associated to the first peak of Mg^{2+}–DNA*p* and Mg^{2+}–PO_4^{3-} is 4.3 Å, which is within the area of the broad peak obtained for DNA*p*-PO_4^{3-}. These results indicate that PO_4^{3-} anions tend to form clusters around the polyphosphate backbone of DNA, repulsive interactions being shielded by the Ca^{2+} and Mg^{2+} ions located between them. This clustering distribution is shown in Figure 3b, which displays a representative snapshot from the MD simulation of the PO_4^{3-} containing system (blue ellipsoid) superposed to that from simulation with Ox^{2-}. Overall, the formation of calcium phosphate clusters surrounding the DNA backbone is fully consistent with previous experimental observation, in which the

DNA was found to act as template for the nucleation and growth of crystalline HAp.[28]

Encapsulation of DNA inside mineral nanopores

In order to elucidate DNA can be present inside HAp and CaOx in microcalcifications, the encapsulation of R1A and DD in mineral nanopores was modelled. Figure 4 represents the structure of R1A and DD dodecamers embedded in HAp and CaOx nanopores after relaxation through energy minimizations and MD, as is described in the Methods section.

In the case of HAp, the DNA double helix occupies practically the whole pore, independently of its methylation degree. Although interactions with mineral ions induce some distortions in the backbone, the DD and R1A double helix with its intra-strand stacking and the inter-strand hydrogen bonds are clearly preserved. This is illustrated in Figure 4, which also depicts the double helix without the mineral. As it can be seen, initial double helices do not undergo significant distortions, which is fully consistent with the simulations discussed in the previous sub-section. Thus, the attractive interaction between the Ca^{2+} ions of HAp and the polyphosphate chain of the DNA allows maintaining the stability of the B-DNA inside the pore. The RMSD between the canonical double helix (*i.e.* the starting structure) and the relaxed double helix, which was calculated considering all the atoms, is relatively small: 1.9 and 3.5 Å for R1A and DD, respectively.

Relaxation of R1A and DD dodecamers embedded in CaOx induced drastic geometric distortions that affected significantly both the inter-strand hydrogen bonds and the intra-strand π-π stacking, as is displayed in Figure 4. Thus, the RMSD calculated with respect to the canonical B-DNA used as starting point was close to 10 Å

for both sequences, which is significantly higher than the values obtained for complexes with HAp. This is because of the repulsive interactions between the Ox^{2-} anions and the phosphate groups of the double helix that, in this case, are not shielded by the attractive interactions of the latter with the Ca^{2+} ions. Apparently, these results indicate that the geometry of CaOx is not appropriated to preserve the tertiary structure of the biological DNA when the latter is embedded inside of the nanopore.

Overall, these results indicate that the cavity generated in HAp allows B-DNA double helices encapsulation without producing mineral-induced stress, while the opposite situation is obtained when CaOx nanopores are studied. Although this feature might be related with the benign and malignancy cancer prognosis associated to CaOx and HAp microcalcifications,[21-22] no experimental observation relating the medical diagnosis and the functionality of the genes linked to cancer disease has been reported yet.

Experimental DNA mineralization

As a consequence of the previous *in silico* results, DNA mineralization with CaOx, magnesium oxalate (MgOx) and HAp was investigated forming DNA-CaOx, DNA-MgOx and DNA-HAp complexes through the procedure described in the Methods section. It is worth noting that DNA was incorporated into aqueous inorganic solutions and, therefore, the biomolecule could be absorbed onto the surface of the formed mineral particles or encapsulated into them. The non-physiological conditions used in these experiments have been used as a proof of concept for the underlying physicochemical mechanism considering monohydrated CaOx and HAp, which are the minerals employed in the simulations. Thus, the conditions used for the in vitro synthesis of minerals have avoided mixed effects of other crystalline forms, as for

example dihydrated and trihydrated in the case of CaOx and brushite, tricalcium phosphate or amorphous calcium phosphate in the case of HAp

Figure 5a compares the UV-vis spectra recorded for: a1) as obtained DNA-CaOx samples; a2) digested DNA-CaOx samples, in which superficially adsorbed DNA is removed by digesting as obtained DNA-CaOx complexes with DNAase; a3) as obtained DNA-CaOx samples from a1 are re-dissolved with sodium citrate (5 mM); and a4) digested DNA-CaOx samples dissolved with sodium citrate (5 mM). The UV-vis spectrum of as prepared DNA-CaOx complexes (a1) clearly demonstrates the presence of DNA since a characteristic absorption peak is observed at 266 nm. However, the absorbance at 266 nm decreases considerably after enzymatic degradation treatment (a2). This absorbance increases after dissolution of the as obtained DNA-CaOx complexes (a3), while it remains very small when the digested samples are dissolved (a4). Overall, these results unambiguously demonstrate that the mineralization of DNA from Ca^{2+}- and Ox^{2-}-containing solutions mainly occurs through the adsorption of the biomolecule on the surface of the formed CaOx particles, whereas the encapsulation of DNA inside such inorganic particles is very limited.

Trying to promote the affinity of Ox^{2-} towards DNA, DNA-MgOx complexes were prepared following the procedure previously used to obtain DNA-CaOx complexes (see Methods section). As the electrostatic binding of Mg^{2+} in the grooves of DNA is essential for the stability of the double helix, substitution of Ca^{2+} by Mg^{2+} was hypothesized to favor the mineralization of DNA. The UV-vis spectra recorded for as prepared, digested and dissolved DNA-MgOx samples are displayed in Figure 5b. Surprisingly, the absorption peak at 266 nm is very small for the as obtained samples, before and after dissolution (b1 and b3, respectively) and inexistent for the digested ones, before and after dissolution (b2 and b4, respectively). Accordingly, the adsorption

of DNA onto the mineral surface is lower for MgOx than for CaOx, whereas the DNA encapsulation was very limited in both cases. These experimental observations are fully consistent with MD simulations on the nucleation of DNA biominerals, in which the formation of DNA*p*$\cdots Ca^{2+}\cdots Ox^{2-}$ and DNA*p*$\cdots Mg^{2+}\cdots Ox^{2-}$ interacting triads were not detected, indicating that Ox^{2-} anions hinder the mineralization of DNA, independently of the identity of the divalent metallic cation.

Conversely, UV-vis spectra obtained for DNA-HAp complexes shows the presence of both DNA absorbed on the surface and encapsulated inside the particles. Thus, the DNA absorption peak is clearly observed in as prepared complexes, before and after dissolution (c1 and c3, respectively) and in samples dissolved after digestion with the DNAase (c4). Interestingly, the absorbance is much higher for dissolved samples (c3 and c4) than that of as prepared samples (c1 and c2), evidencing the very high tendency of HAp to grow surrounding the DNA molecule that acts as the nucleating template.

It is worth noting that the experimental observations achieved for DNA-CaOx, DNA-MgOx and DNA-HAp complexes are fully consistent with the computer simulations discussed above. Thus, MD simulations showed that, although DNA can be adsorbed onto the most stable facets of CaOx and, especially, HAp, its predominant role as nucleating template only occurs for HAp. On the other hand, Mg^{2+} ions tend to be located in the grooves of DNA, acting as counterions of the polyphosphate backbone. Nevertheless, MgOx particles are not appropriated to mineralize the DNA by superficial absorption or encapsulation.

QM calculations

Interactions between the different species involved in DNA-CaOx complexes were further studied to completely understand the poor affinity of DNA by CaOx in

comparison to HAp. For this purpose, QM calculations in vacuum and within the framework of an implicit solvation model were performed on small representative model complexes involving two or three interacting species, which are depicted in Figure 6. The estimated ΔG_b and ΔG_{hyd} values, which were calculated as is indicated in the Methods section, are expected to complete the scenario described by classical MD simulations. The ΔG_b informs about the strength of the interactions that maintain the species involved in the complex assembled in aqueous solution, while ΔG_{hyd} gives the free energy change associated with the transfer of the complex between vacuum and bulk water. The ΔG_b and ΔG_{hyd} values included in Figure 6 completely support the conclusions derived from MD simulations and experimental observations.

First inspection of the ΔG_b and ΔG_{hyd} values reveals that the strength of the binding is more exothermic in complexes with Mg^{2+} than with Ca^{2+}, whereas hydration favors the latter with respect to the former. Careful analysis reveals that when differential energies are considered for the calculated complexes, this behavior can be explained. The ΔG_b is more attractive for $Mg^{2+}\cdots$DNA*p* than for $Ca^{2+}\cdots$DNA*p* (*i.e.* $\Delta\Delta G_b$= -32.5 kcal/mol), indicating that the phosphates from DNA tend to coordinate Mg^{2+} instead of Ca^{2+} when both ions are present. The same trend is observed for $Mg^{2+}\cdots Ox^{2-}$ and $Ca^{2+}\cdots Ox^{2-}$ complexes, the strength of the binding being higher in the former than in the latter (*i.e.* $\Delta\Delta G_b$= -46.0 kcal/mol). However, ΔG_{hyd} indicates the opposite, the solvation being significantly more favored for complexes with Ca^{2+} than with Mg^{2+} (*i.e.* $\Delta\Delta G_{hyd}$= -42.0 and -49.5 kcal/mol for complexes with DNA*p* and Ox^{2-}, respectively). The balance between $\Delta\Delta G_b$ and $\Delta\Delta G_{hyd}$ values indicates that, in a solution containing all the considered species, Ox^{2-} preferentially interacts with Ca^{2+} while DNA phosphate prefers Mg^{2+}.

Additional calculations on model complexes involving three interacting species provide complete understanding of the *in lab* experiments described in the previous sub-section for CaOx and MgOx. Thus, the strength of the binding in $Ox^{2-}\cdots Mg^{2+}\cdots Ox^{2-}$ is stronger than in $Ox^{2-}\cdots Ca^{2+}\cdots Ox^{2-}$ by $\Delta\Delta G_b$= -33.4 kcal/mol, while the hydration of the latter is favored with respect to that of the former by $\Delta\Delta G_{hyd}$= -40.1 kcal/mol. Therefore, the sum of these free energy gaps indicates that Ox^{2-} anions tend to surround and coordinate with Ca^{2+} instead of Mg^{2+}. Amazingly, this tendency is much more pronounced for DNA*p*$\cdots Mg^{2+}\cdots Ox^{2-}$ and DNA*p*$\cdots Ca^{2+}\cdots Ox^{2-}$ complexes. Thus, although the binding is favored in the former complex by $\Delta\Delta G_b$= -35.0, hydration stabilizes the latter by $\Delta\Delta G_{hyd}$= -60.2 kcal/mol. These and the previous $\Delta\Delta G_b$ and $\Delta\Delta G_{hyd}$ differences indicate that the coordination of an extra Ox^{2-} with already Ox^{2-}-bound Ca^{2+} or Mg^{2+} instead of DNA*p*-bound Mg^{2+} is favored before the precipitation of any of the complexes may happen. In addition, $Ca^{2+}\cdots Ox^{2-}$ and $Ox^{2-}\cdots Ca^{2+}\cdots Ox^{2-}$ have much more favorable hydration than their corresponding Mg^{2+} counterparts. Finally, Mg^{2+} prefers to coordinate with two Ox^{2-} rather than with DNA*p* and Ox^{2-}, which enables CaOx and MgOx calcifications to grow DNA-free in the solution as previously confirmed by *in the lab* tests.

CONCLUSIONS

In summary, we systematically compared the mineralization of DNA in CaOx and HAp using a synergistic computational-experimental approach. Being the latter materials traditionally related with transfection of cells with nucleic acids and with the formation of microcalcifications inside of living organisms, the biomedical application of DNA-based biominerals might be further improved by understanding the fundamental interactions associated to adsorption and encapsulation of such

biomolecule in HAp and CaOx. Using atomistic MD simulations, we studied DNA adsorption and encapsulation in CaOx and HAp. Although DNA can be adsorbed onto the most stable facet of the two minerals, important differences are found. HAp is able to preserve the DNA double helix because of the complementarity between their phosphate anions through isomorphic planes, while the repulsive interactions between the oxalate anions of CaOx and the polyphosphate backbone of the biomolecule cause the destabilization of the double helix. Besides, DNA nucleates the growing of HAp when it is immersed in an ionic solution containing Ca^{2+}, Mg^{2+} and PO_4^{3-} ions and encapsulates it inside HAp nanopores maintaining the stability of the double helix. The opposite behavior is observed when DNA is immersed in a Ca^{2+}, Mg^{2+} and Ox^{2-} solution and encapsulated in CaOx pores: the minerals grow separately from DNA and the double helix undergoes severe structural alterations, respectively. These theoretical results have been corroborated experimentally by preparing DNA-HAp, DNA-CaOx and DNA-MgOx complexes. UV-vis spectra show that HAp is much more effective than CaOx and MgOx for DNA mineralization in terms of both adsorption and encapsulation. Furthermore, QM calculations on model complexes in aqueous solution show that Ca^{2+} ions prefer to coordinate with two Ox^{2-} than form triads involving an Ox^{2-} and a phosphate group from DNA.

Another fundamental insight obtained in this work is that results described above are independent of the methylation degree of the simulated DNA dodecamers. This is very relevant in the medical context since CaOx and HAp breast cancer micro-calcifications have been associated with more frequent benign and malign prognosis, respectively. Results derived from this study open a new concept that deserves further research, suggesting that HAp microcalcifications might be involved in the protection and transport of carcinogenic DNA.

ACKNOWLEDGEMENTS

Authors acknowledge MINECO-FEDER (RTI2018-098951-B-I00 and RTI2018-101827-B-I00), Agència de Gestió d'Ajuts Universitaris i de Recerca (2017SGR359 and 2017SGR373) and B. Braun Surgical, S.A. for financial support. This work is integrated within a wider research project supported by B. Braun Surgical S.A., UPC, ICS and ICFO. Support for the research of C.A. was received through the prize "ICREA Academia" for excellence in research funded by the Generalitat de Catalunya.

REFERENCES

(1) Tan, L. H.; Xing, H.; Lu, Y. DNA as a Powerful Tool for Morphology Control, Spatial Positioning, and Dynamic Assembly of Nanoparticles. *Acc. Chem. Res.* **2014**, *47*, 1881−1890.

(2) Zhou, W.; Saran, R.; Liu, J. Metal Sensing by DNA. *Chem. Rev.* **2017**, *117*, 8272−8325.

(3) Wang, H.; Yang, R.; Yang, L.; Tan, W. Nucleic Acid Conjugated Nanomaterials for Enhanced Molecular Recognition. *ACS Nano* **2009**, *3*, 2451−2460.

(4) Giljohann, D. A.; Seferos, D. S.; Daniel, W. L.; Massich, M. D.; Patel, P. C.; Mirkin, C. A. Gold Nanoparticles for Biology and Medicine. *Angew. Chem., Int. Ed.* **2010**, *49*, 3280−3294.

(5) Jones, M. R.; Seeman, N. C.; Mirkin, C. A. Programmable Materials and the Nature of the DNA Bond. *Science* **2015**, *347*, 1260901.

(6) Song, S.; Qin, Y.; He, Y.; Huang, Q.; Fan, C.; Chen, H.-Y. Functional Nanoprobes for Ultrasensitive Detection of Biomolecules. *Chem. Soc. Rev.* **2010**, *39*, 4234−4243.

(7) Liu, B.; Salgado, S.; Maheshwari, V.; Liu, J. DNA Adsorbed on Graphene and Graphene Oxide: Fundamental Interactions, Desorption and Applications. *Curr. Opin. Colloid Interface Sci.* **2016**, *26*, 41−49.

(8) Pautler, R.; Kelly, E. Y.; Huang, P.-J. J.; Cao, J.; Liu, B.; Liu, J. Attaching DNA to Nanoceria: Regulating Oxidase Activity and Fluorescence Quenching. *ACS Appl. Mater. Interfaces* **2013**, *5*, 6820−6825.

(9) Narasaraju, T. S. B.; Phebe, D. E. Some Physico-Chemical Aspects of Hydroxylapatite. *J. Mater. Sci.* **1996**, *31*, 1−21.

(10) Weiner, S.; Wagner, H. D. THE MATERIAL BONE: Structure-Mechanical Function Relations. *Annu. Rev. Mater. Sci*. **1998**, *28*, 271−298.

(11) Fratzl, P.; Gupta, H. S.; Paschalis, E. P.; Roschger, P. Structure and Mechanical Quality of the Collagen–Mineral Nano-Composite in Bone. *J. Mater.Chem.* **2004**, *14*, 2115−2123.

(12) Uskoković, V.; Uskoković, D. P. Nanosized Hydroxyapatite andOther Calcium Phosphates: Chemistry of Formation and Application as Drug and Gene Delivery Agents. *J. Biomed. Mater. Res., Part B* **2011**, *96B*, 152−191.

(13) Kozlova, D.; Chernousova, S.; Knuschke, T.; Buer, J.; Westendorf, A. M.; Epple, M. Cell Targeting by Antibody-Functionalized Calcium Phosphate Nanoparticles. *J. Mater. Chem.* **2012**, *22*, 396−404.

(14) Olton, D.; Li, J.; Wilson, M.E.; Rogers, T.; Close, J.; Huang, L.; Kumta, P.N.; Sfeir, C. Nanostructured Calcium Phosphates (NanoCaPs) for Non-Viral Gene Delivery: Influence of the Synthesis Parameters on Transfection Efficiency. *Biomaterials* **2007**, *28*, 1267–1279.

(15) Wan, Y.; Wu, C.; Zuo, G.; Xiong, G.; Jin, J.; Guo, R.; Wang, Z.; Luo, H. Controlled Template Synthesis of Lamellar Hydroxyapatite Nanoplates as a Potential Carrier for Gene Delivery. *Mater. Chem. Phys.* **2015**, *156*, 238−246.

(16) Andrews-Pfannkoch, C.; Fadrosh, D. W.; Thorpe, J.; Williamson, S. J. Hydroxyapatite-Mediated Separation of Double-Stranded DNA, Single-Stranded DNA, and RNA Genomes from Natural Viral Assemblages. *Appl. Environ. Microb.* **2010**, *76*, 5039−5045.

(17) Baker, R.; Rogers, K. D.; Shepherd, N.; Stone, N. New Relationships between Breast Microcalcifications and Cancer. *British J. Cancer* **2010**, *103*, 1034−1039.

(18) Haka, A. S.; Shafer-Peltier, K. E.; Fitzmaurice, M.; Crowe, J.; Dasari, R. R.; Feld, M. S. Diagnosing Breast Cancer by Using Raman Spectroscopy. *Proc. Natl. Acad. Sci*. **2005**, *102*, 12371–12376.

(19) Haka, A. S.; Shafer-Peltier, K. E.; Fitzmaurice, M.; Crowe, J.; Dasari, R. R.; Feld, M. S. Identifying Microcalcifications in Benign and Malignant Breast Lesions by Probing Differences in Their Chemical Composition using Raman Spectroscopy. *Cancer Res.* **2002**, *62*, 5375–5380.

(20) Tse, G. M.; Tan, P.-H. Cheung, H. S.; Chu, W. C.; Lam, W. W. Intermediate to Highly Suspicious Calcification in Breast Lesions: A Radio-Pathologic Correlation. *Breast Cancer Res. Treat.* **2008**, *110*,1–7.

(21) Frappart, L.; Boudeulle, M.; Boumendil, J.; Lin, H. C.; Martinon, I.; Palayer, C.; Mallet-Guy, Y.; Raudrant, D.; Bremond, A.; Rochet, Y. Structure and Composition of Microcalcifications in Benign and Malignant Lesions of the Breast: Study by Light Microscopy, Transmission and Scanning Electron Microscopy, Microprobe Analysis, and X-Ray Diffraction. *Hum. Pathol*. **1984,** *15*, 880–889.

(22) Cox, R. F.; Hernandez-Santana, A.; Ramdass, S.; McMahon, G.; Harmey, J. H.; Morgan, M. P. Microcalcifications in Breast Cancer: Novel Insights into the Molecular Mechanism and Functional Consequence of Mammary Mineralisation. *Br. J. Cancer* **2012,** *106*, 3, 525–537.

(23) del Valle, L. J.; Bertran, O.; Chaves, G.; Revilla-López, G.; Rivas, M.; Casas, M. T.; Casanovas, J.; Turon, P.; Puiggalí, J.; Alemán, C. DNA Adsorbed on Hydroxyapatite Surfaces. *J. Mater. Chem.* **2014**, *2*, 6953–6966.

(24) Rivas, M.; Casanovas, J.; del Valle, L. J.; Bertran, O.; Revilla-López, G.; Turon, P.; Puiggalí, J.; Alemán, C. An Experimental-Computer Modeling Study of Inorganic Phosphates Surface Adsorption on Hydroxyapatite Particles. *Dalton Trans.* **2015**, *44*, 9980–9991.

(25) Revilla-López, G.; Casanovas, J.; Bertran, O.; Turon, P.; Puiggalí, J.; Alemán, C. Modeling Biominerals Formed by Apatites and DNA. *Biointerphases* **2013**, *8*, 10.

(26) Takeshita, T.; Matsuura, Y.; Arakawa, S.; Okamoto, M. Biomineralization of Hydroxyapatite on DNA Molecules in SBF: Morphological Features and Computer Simulation. *Langmuir* **2013**, *29*, 11975–11981.

(27) Vasconcellos, K. B.; McHugh, S. M.; Dapsis, K. J.; Petty, A. R.; Gerdon, A. E. Biomimetic Nanoparticles with Polynucleotide and PEG Mixed-Nonolayers Enhance Calcium Phosphate Mineralization. *J. Nanopart. Res.*, 2013, **15**, 1942.

(28) Bertran, O.; del Valle, L. J.; Revilla-López, G.; Chaves, G.; Cardus, L.; Casas, M. T.; Casanovas, J.; Turon, P.; Puiggalí, J.; Alemán, C. Mineralization of DNA into Nanoparticles of Hydroxyapatite. *Dalton Trans.* **2014**, *43*, 317–327.

(29) Klesing, J.; Chernousova, S.; Epple, M. Freeze-Dried Cationic Calcium Phosphate Nanorods as Versatile Carriers of Nucleic Acids (DNA, siRNA). *J. Mater. Chem.* **2012**, *22*, 199–204

(30) Wu, G. J.; Zhou, L. Z.; Wang, K. W.; Chen, F.; Sun, Y.; Duan, Y. R.; Zhu, Y. J.; Gu, H. C. Hydroxylapatite Nanorods: An Efficient and Promising Carrier for Gene Transfection. *J. Colloid Interface Sci.* **2010**, *345*, 427–432.

(31) Zhu, S. H.; Huang, B. Y.; Zhou, K. C.; Huang, S. P.; Liu, F.; Li, Y. M.; Xue, Z. G.; Long, Z. G. Hydroxyapatite Nanoparticles As a Novel Gene Carrier. *J. Nanopart. Res.* **2004**, *6*, 307–311.

(32) Bertran, O.; del Valle, L. J.; Revilla-López, G. Rivas, M.; Chaves, M.; Casas, M. T.; Casanovas, J.; Turon, P.; Puiggalí, J.; Alemán, C.Synergistic Approach to Elucidate the Incorporation of Magnesium Ions into Hydroxyapatite. *Chem. Eur. J.* **2015**, *21*, 2537–2546.

(33) Betran, O.; Revilla-López, G.; Casanovas, J.; del Valle, L. J.; Turon, P.; Puiggalí, J.; Alemán, C. Dissolving Hydroxyolite: A DNA Molecule into Its Hydroxyapatite Mold. *Chem. Eur. J.* **2016**, *22*, 6631–6636.

(34) Phillips, J. C.; Braun, R.; Wang, W.; Gumbart, J.; Tajkhorshid, E.; Villa, E.; Chipot, C.; Skeel, R. D.; Kalé, L.; Schulten, K. Scalable Molecular Dynamics with NAMD. *J. Comput. Chem.* **2005**, *26*, 1781–1802.

(35) Fleischer, T.; Tekpli, X.; Mathelier, A.; Wang, S.; Nebdal, D.; Dhakal, H. P.; Kleivi, K.; Sahlberg, K. K.; Schlichting, E; Oslo Breast Cancer Research Consortium (OSBREAC); Børresen-Dale, A. L.; Borgen, E.; Naume, B.; Eskeland, R.; Frigessi, A.; Tost, J.; Hurtado, A.; Kristensen, V. N. DNA Methylation at Enhancers Identifies Distinct Breast Cancer Lineages. *Nat. Commun.* **2017**, *8*, 1379.

(36) Si, X.; Zhao, Y.; Yang, C.; Zhang, S.; Zhang, X. DNA Methylation as a Potential Diagnosis Indicator for Rapid Discrimination of Rare Cancer Cells and Normal Cells. *Sci. Rep.* **2015**, *5*, 11882.

(37) Widschwendter, M.; Jones, P. A. DNA Methylation and Breast Carcinogenesis. *Oncogene* **2002**, *21*, 5462–5482.

(38) Mathe, A.; Wong-Brown, M.; Locke, W. J.; Stirzaker, C.; Braye, S. G.; Forbes, J. F.; Clark, S. J.; Avery-Kiejda, K. A.; Scott, R. J. DNA Methylation Profile of Triple Negative Breast Cancer-Specific Genes Comparing Lymph Node Positive Patients to Lymph Node Negative Patients. *Sci. Rep.* **2016**, *6*, 33435.

(39) Dammann, R.; Yang, G.; Pfeifer, G. P. Hypermethylation of the cpG Island of Ras Association Domain Family 1A (RASSF1A), a Putative Tumor Suppressor Gene from the 3p21.3 Locus, Occurs in a Large Percentage of Human Breast Cancers. *Cancer Res.* **2001**, *61*, 3105–3109.

(40) Gueroult, M.; Boittin, O.; Mauffret, O.; Etchebest, C.; Hartmann, B. Charge Neutralization was Performed with the Addition of Na^+ Counterions. *PLoS One* **2012**, *7*, e41704.

(41) Duan, Y.; Wu, C.; Chowdhury, S.; Lee, M. C.; Xiong, G.; Zhang, W.; Yang, R.; Cieplak, P.; Luo, R.; Lee, T.; Caldwell, J.; Wang, J.; Kollman, P. A. Point-Charge Force Field for Molecular Mechanics Simulations of Proteins Based on Condensed-Phase Quantum Mechanical Calculations. *J. Comput. Chem.* **2003**, *24*, 1999–2012.

(42) Bradbrook, G. M.; Gleichmann, T.; Harrop, S. J.; Habash, J.; Raftery, J.; Kalb, J.; Yariv J.; Hillier I. H.; Helliwell, J. R. X-Ray and Molecular Dynamics Studies of Concanavalin-A Glucoside and Mannoside Complexes. Relating Structure to Thermodynamics of Binding. *J. Chem. Soc., Faraday Trans.* **1998**, *94*, 1603–1611.

(43) Allnér, O.; Nilsson, L.; Villa, A. Magnesium Ion–Water Coordination and Exchange in Biomolecular Simulations. *J. Chem. Theor. Comput.* **2012**, *8*, 1493–1502.

(44) Jorgensen, W. L.; Chandrasekhar, J.; Madura, J. D.; Impey, R. W.; Klein, M. L. Comparison of Simple Potential Functions for Simulating Liquid Water. *J. Chem. Phys.* **1983**, *79*, 926–935.

(45) Wang, J.; Wolf, R. M.; Caldwell, J. W.; Kollman, P. A.; Case, D. A. Development and Testing of a General Amber Force Field. *J. Comput. Chem.* **2004**, *25*, 1157–1174.

(46) Bayly, C. I.; Cieplak, P.; Cornell, W.; Kollman, P. A. A Well-Behaved Electrostatic Potential Based Method Using Charge Restraints for Deriving Atomic Charges: The RESP Model. *J. Phys. Chem.* **1993**, *97*, 10269v10280.

(47) Berendsen, H. J.; Postma, J. V.; van Gunsteren, W. F.; DiNola, A. R. H. J.; Haak, J. R. Molecular Dynamics with Coupling to an External Bath. *J. Chem. Phys.* **1984**, *81*, 3684–3690.

(48) Darden, T.; York, D.; Pedersen, L. Particle Mesh Ewald: An N·log (N) Method for Ewald sums in Large Systems. *J. Chem. Phys.* **1993**, *98*, 10089–10092

(49) Ryckaert, J. P.; Ciccotti, G.; & Berendsen, H. J. Numerical Integration of the Cartesian Equations of Motion of a System with Constraints: Molecular Dynamics of *n*-Alkanes. *J. Comput. Phys.* **1977**, *23*, 327–341.

(50) Stork, L.; Muller, P.; Dronskowski, R.; Ortlepp, J. R. *Z. Kristallogr.* **2005**, *220*, 201–205.

(51) Daudon, M.; Bazin, D.; André, G.; Jungers, P.; Cousson, A.; Chevallier, P.; Veéron, E.; Matzen, G. Examination of Whewellite Kidney Stones by Scanning Electron Microscopy and Powder Neutron Diffraction Techniques. *J. Appl. Cryst.* **2009**, *42*, 109–115.

(52) M Frisch, M. J.; Trucks, G. W.; Schlegel, H. B.; Scuseria, G. E.; Robb, M. A.; Cheeseman, J. R.; Scalmani, G.; Barone, V.; Mennucci, B.; Petersson, G. A.; Nakatsuji, H.; Caricato, M.; Li, X.; Hratchian, H. P.; Izmaylov, A. F.; Bloino, J.; Zheng, G.;

Sonnenberg, J. L.; Hada, M.; Ehara, M.; Toyota, K.; Fukuda, R.; Hasegawa, J.; Ishida, M.; Nakajima, T.; Honda, Y.; Kitao, O.; Nakai, H.; Vreven, T.; J. A. Montgomery Jr.; Peralta, J. E.; Ogliaro, F.; Bearpark, M.; Heyd, J. J.; Brothers, E.; Kudin, K. N.; Staroverov, V. N.; Kobayashi, R.; Normand, J.; Raghavachari, K.; Rendell, A.; Burant, J. C.; Iyengar, S. S.; Tomasi, J.; Cossi, M.; Rega, N.; Millam, J. M.; Klene, M.; Knox, J. E.; Cross, J. B.; Bakken, V.; Adamo, C.; Jaramillo, J.; Gomperts, R.; Stratmann, R. E.; Yazyev, O.; Austin, A. J.; Cammi, R.; Pomelli, C.; Ochterski, J. W.; Martin, R. L.; Morokuma, K.; Zakrzewski, V. G.; Voth, G. A.; Salvador, P.; Dannenberg, J. J.; Dapprich, S.; Daniels, A. D.; Farkas, Ö.; Foresman, J. B.; Ortiz, J. V.; Cioslowski, J.; Fox, D. J. Gaussian 09, Revision A.1. Gaussian, Inc.: Wallingford CT, **2009**.

(53) Becke, A. D. Density-Functional Thermochemistry. III. The Role of Exact Exchange. *J. Chem. Phys*. **1993**, *98*, 5648–5652.

(54) Lee, C.; Yang, W.; Parr, R. G. Development of the Colle-Salvetti Correlation-Energy Formula into a Functional of the Electron Density. *Phys. Rev. B: Condens. Matter*. **1988**, *37*, 785–789.

(55) Marenich, A. V.; Cramer, C. J.; Truhlar, D. G. Universal Solvation Model Based on Solute Electron Density and on a Continuum Model of the Solvent Defined by the Bulk Dielectric Constant and Atomic Surface Tensions. *J. Phys. Chem. B* **2009**, 113, 6378–6396.

(56) Mkhonto, D.; de Leeuw, N. H. A Computer Modelling Study of the Effect of Water on the Surface Structure and Morphology of fFluorapatite: Introducing a $Ca_{10}(PO_4)_6F_2$ Potential Model. *J. Mater. Chem.* **2002**, *12*, 2633–2642.

(57) Di Tommaso, D.; Hernández, S. E. R.; Du, Z.; de Leeuw, N. H. Density Functional Theory and Interatomic Potential Study of Structural, Mechanical and Surface Properties of Calcium Oxalate Materials. *RSC Adv.* **2012**, *2*, 4664–4674.

(58) Almora-Barrios, N.; Austen, K. F.; de Leeuw, N. H. Density Functional Theory Study of the Binding of Glycine, Proline, and Hydroxyproline to the Hydroxyapatite (0001) and (0110) Surfaces. *Langmuir* **2009**, *25*,5018–5025.

(59) Filgueiras, M. R. T.; Mkhonto, D.; de Leeuw, N. H. Computer Simulations of the Adsorption of Citric Acid at Hydroxyapatite Surfaces. *J. Cryst. Growth* **2006**, *294*, 60–68.

(60) de Leeuw, N. H.; Rabone, J. A. L. Molecular Dynamics Simulations of the Interaction of Citric Acid with the Hydroxyapatite (0001) and (011¯0) Surfaces in an Aqueous Environment. *CrystEngComm* **2007**, *9*, 1178–1186.

(61) Sandersius, S.; Rez, P. Morphology of Crystals in Calcium Oxalate Monohydrate Kidney Stones. *Urol. Res.* **2007**, *35*, 287-293.

(62) Sheng, X. X.; Jung, T. S.; Wesson, J. A.; Ward, M. D. Adhesion at Calcium Oxalate Crystal Surfaces and the Effect of Urinary Constituents. *Proc. Natl. Acad. Sci.* **2005**, *102*, 267–272.

CAPTIONS TO FIGURES

Figure 1. Axial and equatorial perspectives of the starting models used to represent the DD double helix embedded in HAp and CaOx nanopores.

Figure 2. Comparison of DNA adsorption on HAp and monohydrated CaOx. Temporal evolution of the RMSD with respect to the canonical B-DNA double helix for (a) R1A (5'-CG^{4}GTCG^{5}CCG^{6}TCG^{7}-3') and (b) DD (5'-CGCGAATTCGCG-3') adsorbed onto the (001) HAp and (100) CaOx facets. The RMSD obtained for the DNA in aqueous solution has been included for comparison. Axial view of the R1A dodecamer adsorbed onto (c) the (001) surface of HAp and (d) the (100) surface of monohydrated CaOx. Oversized black balls highlight the position of carbon of methyl groups in the methylated DNA. For each system, the axial and equatorial views of the canonical double helix (in black) and the R1A double helix adsorbed onto the HAp or CaOx surface (in red) are compared at the bottom.

Figure 3. (a) RDFs extracted from the MD simulation of the solution containing R1A, water, Mg^{2+}, Ca^{2+} and Ox^{2-}. DNA*p* refers to the DNA phosphate backbone. (b) Superposed snapshot extracted from the simulations with Ox^{2-} (red box) and PO_4^{3-} (blue ellipsoid) ions. (c) RDFs extracted from the MD simulation of the solution containing R1A, water, Mg^{2+}, Ca^{2+} and PO_4^{3-}. In order to ensure that R1A···ion and ion···ion interactions had enough time for their formation (if possible), RDFs were calculated in all cases considering only the last 50 ns of productive simulations.

Figure 4. Axial perspective of the R1A and DD double helix embedded in HAp and CaOx nanopores after relaxation through energy minimization and MD. The double helix is also displayed without mineral to show the different degree of distortion induced by the minerals.

Figure 5. UV-vis absorption spectra of the (a) DNA-CaOx, (b) DNA-MgOx and (c) DNA-HAp complexes. Spectra of: as prepared samples (#1, blue solid lines); samples digested with DNAase to eliminate DNA adsorbed on the surface (#2, red solid lines); dissolved as prepared samples (#3, blue dashed lines); and dissolved digested samples (#4, red dashed lines), where # refers to a, b or c.

Figure 6. Quantum mechanics calculated binding free energy in aqueous solution (ΔG_b; kcal/mol) and hydration free energy (ΔG_{hyd}; kcal/mol) for different complexes including either Ca^{2+} or Mg^{2+}, oxalate (Ox^{2-}) and DNA phosphates (*p*DNA): black color letters stands for Ca^{2+} whereas red color ones for Mg^{2+}. Calculations were performed within the SMD-B3LYP/6-311G++(2d,2p) framework.

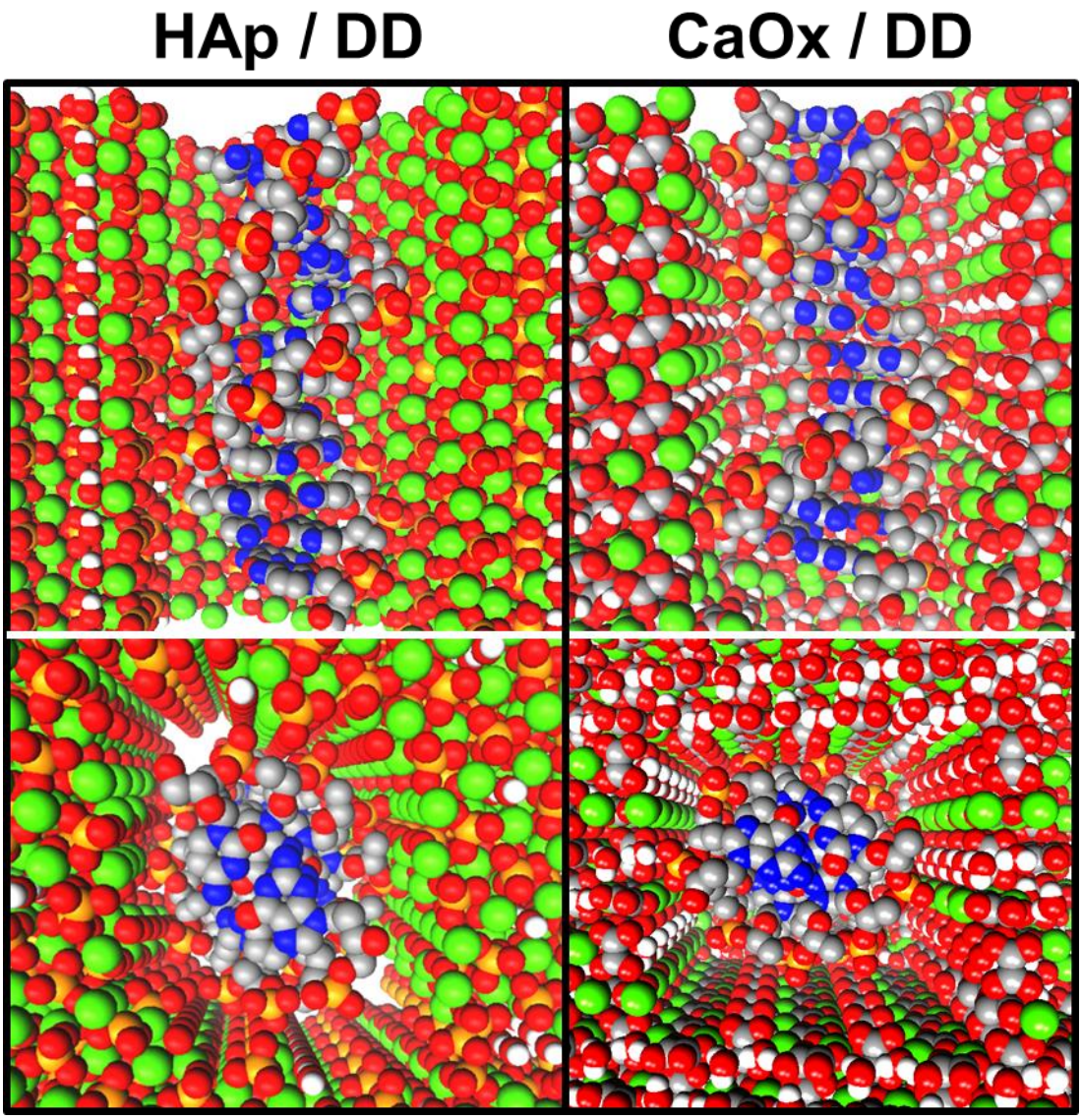

Figure 1

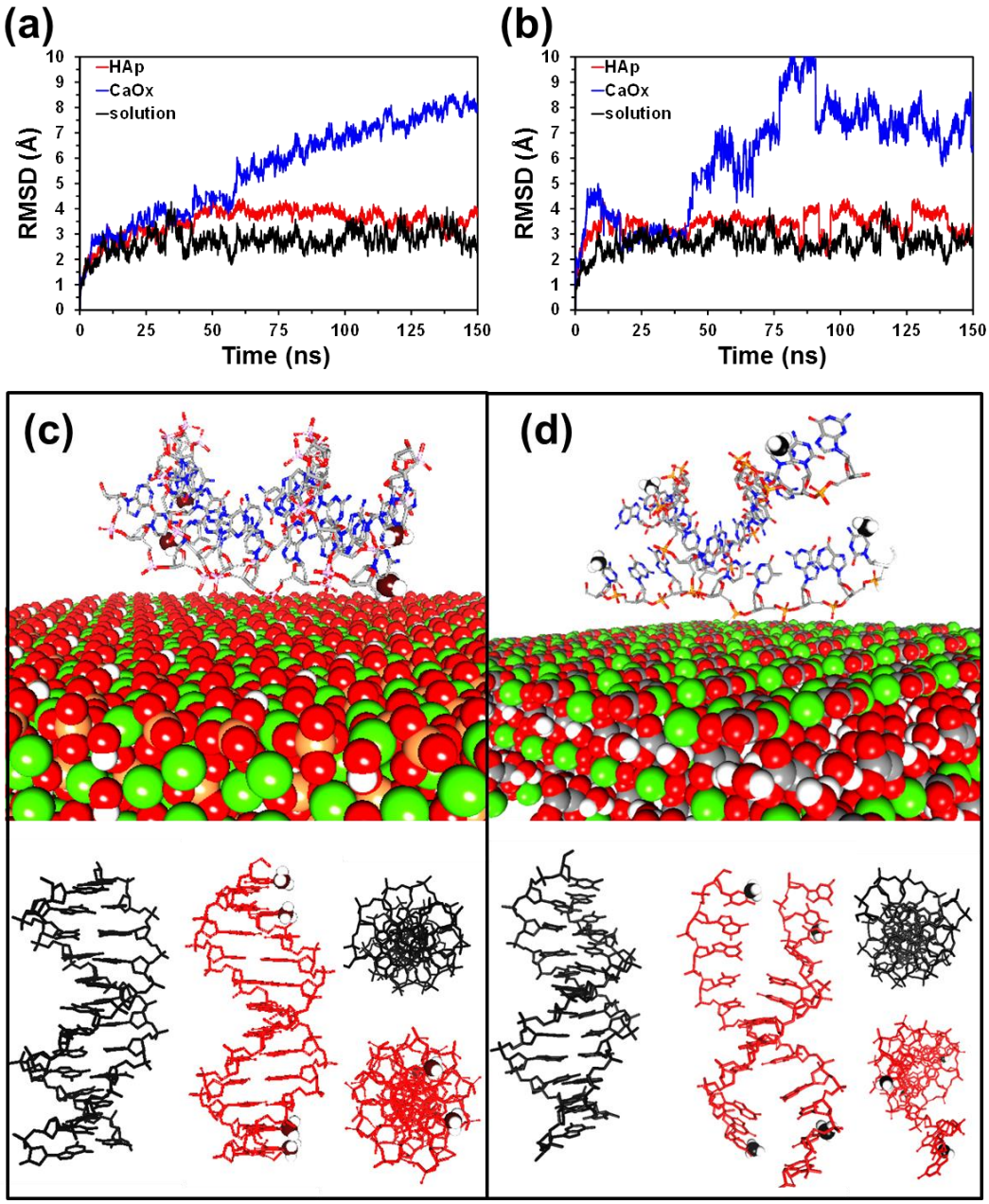
(a)
HAp
CaOx
solution
RMSD (Å)
Time (ns)
(b)
HAp
CaOx
solution
RMSD (Å)
Time (ns)
(c)
(d)

Figure 2

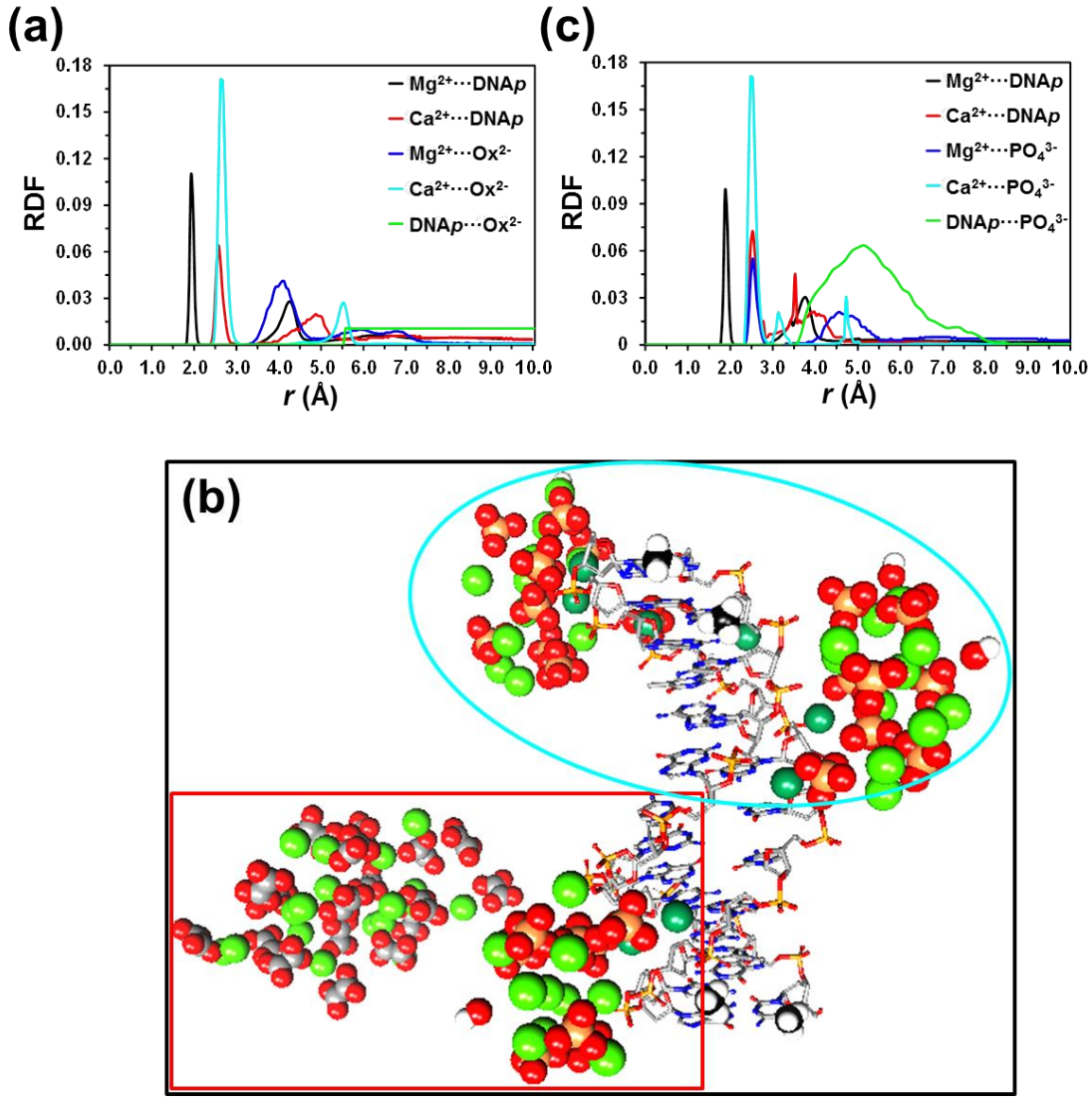
(a)
RDF
r (Å)
Mg2+···DNAp
Ca2+···DNAp
Mg2+···Ox2-
Ca2+···Ox2-
DNAp···Ox2-
(c)
RDF
r (Å)
Mg2+···DNAp
Ca2+···DNAp
Mg2+···PO43-
Ca2+···PO43-
DNAp···PO43-
(b)

Figure 3

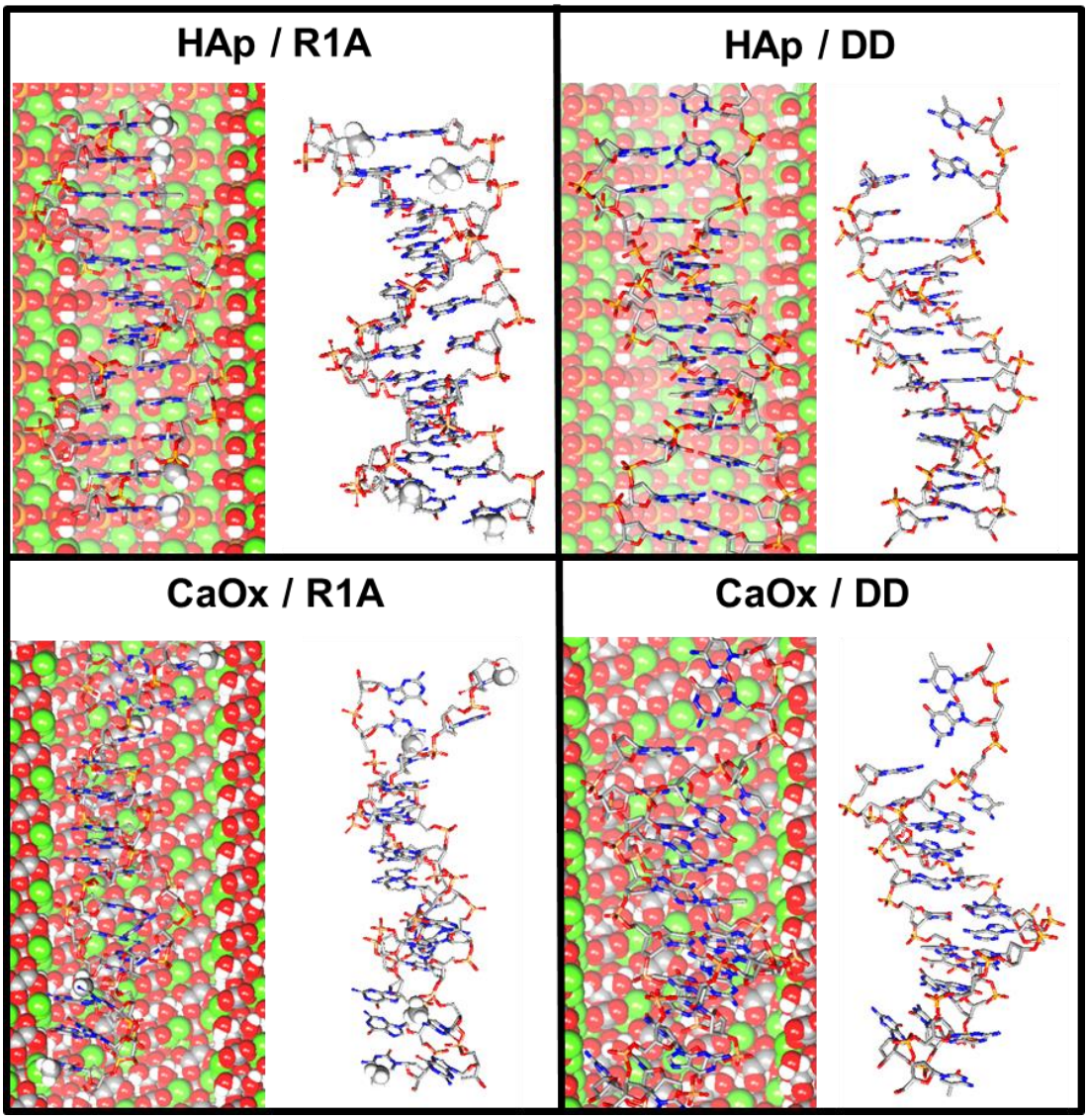

Figure 4

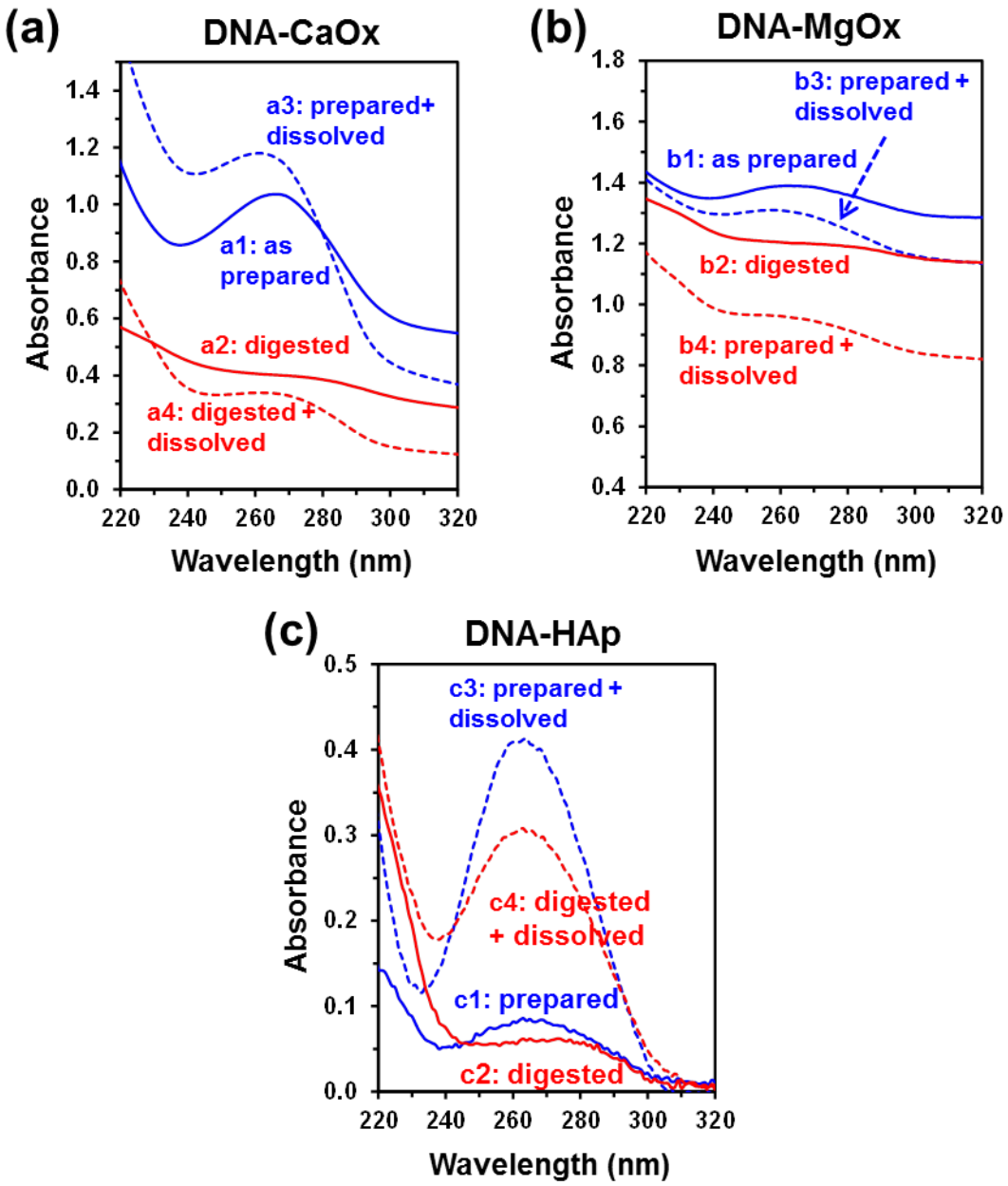
(a)
DNA-CaOx
Absorbance
Wavelength (nm)
a3: prepared+ dissolved
a1: as prepared
a2: digested
a4: digested + dissolved
(b)
DNA-MgOx
Absorbance
Wavelength (nm)
b3: prepared + dissolved
b1: as prepared
b2: digested
b4: prepared + dissolved
(c)
DNA-HAp
Absorbance
Wavelength (nm)
c3: prepared + dissolved
c4: digested + dissolved
c1: prepared
c2: digested

Figure 5

$Ca^{2+}\cdots Ox^{2-}$ / $Mg^{2+}\cdots Ox^{2-}$

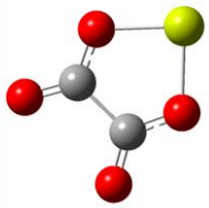

ΔG_b= -143.9 / -189.0
ΔG_{hyd}= -137.7 / -88.2

$DNAp\cdots Ca^{2+}\cdots Ox^{2-}$

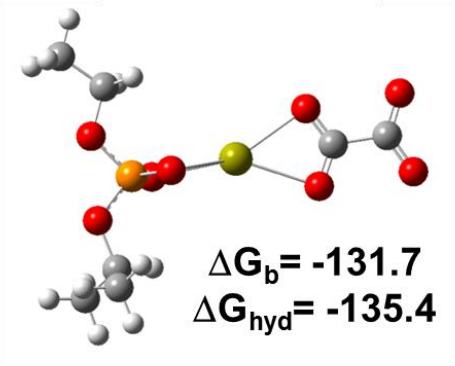

ΔG_b= -131.7
ΔG_{hyd}= -135.4

$Ox^{2-}\cdots Ca^{2+}\cdots Ox^{2-}$

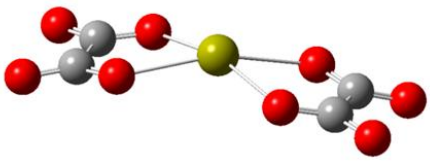

ΔG_b= -137.6
ΔG_{hyd}= -215.6

$DNAp\cdots Ca^{2+}$ / $DNAp\cdots Mg^{2+}$

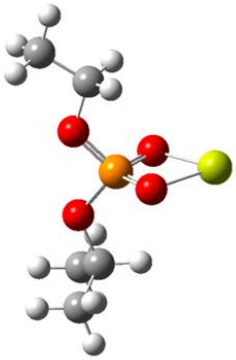

ΔG_b= -2.9 / -35.4
ΔG_{hyd}= -158.1 / -116.1

$DNAp\cdots Mg^{2+}\cdots Ox^{2-}$

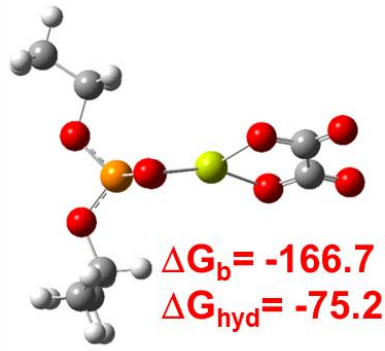

ΔG_b= -166.7
ΔG_{hyd}= -75.2

$Ox^{2-}\cdots Mg^{2+}\cdots Ox^{2-}$

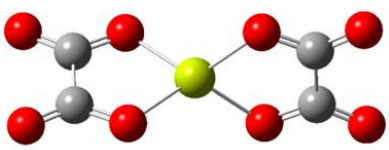

ΔG_b= -171.0
ΔG_{hyd}= -175.5

Figure 6

TOC